



HAL
open science

Ab initio modeling of slip activity in body-centered cubic chromium

Baptiste Bienvenu, Emmanuel Clouet

► **To cite this version:**

Baptiste Bienvenu, Emmanuel Clouet. Ab initio modeling of slip activity in body-centered cubic chromium. *Acta Materialia*, 2022, 224, pp.117485. 10.1016/j.actamat.2021.117485 . cea-03646746

HAL Id: cea-03646746

<https://cea.hal.science/cea-03646746>

Submitted on 19 Apr 2022

HAL is a multi-disciplinary open access archive for the deposit and dissemination of scientific research documents, whether they are published or not. The documents may come from teaching and research institutions in France or abroad, or from public or private research centers.

L'archive ouverte pluridisciplinaire **HAL**, est destinée au dépôt et à la diffusion de documents scientifiques de niveau recherche, publiés ou non, émanant des établissements d'enseignement et de recherche français ou étrangers, des laboratoires publics ou privés.

Ab initio modeling of slip activity in body-centered cubic chromium

Baptiste Bienvenu^a, Emmanuel Clouet^{a,*}

^a Université Paris-Saclay, CEA, Service de Recherches de Métallurgie Physique, F-91191 Gif-sur-Yvette, France

Abstract

Slip activity in body-centered cubic chromium is modeled by means of *ab initio* calculation of screw dislocations core properties and Peierls potential. As dislocations having $1/2\langle 111 \rangle$ Burgers vector and also $\langle 100 \rangle$, both gliding in $\{110\}$ crystallographic planes have been reported experimentally, both screw dislocations are modeled. A generalized yield criterion incorporating physical ingredients necessary to account for deviations from the Schmid law is obtained for $\langle 111 \rangle\{110\}$ and $\langle 100 \rangle\{110\}$ slip systems. We report a broad range of crystal orientations for which $\langle 100 \rangle$ screw dislocations are easier to activate than the conventional $1/2\langle 111 \rangle$ in tension and compression. These results hold for both the non-magnetic and antiferromagnetic phases of body-centered cubic chromium, with only a marginal effect of magnetism.

Keywords: Dislocations, Plasticity, Chromium, Magnetism

1. Introduction

Among all body-centered cubic (bcc) metals, chromium (Cr) is the only one with an antiferromagnetic (AF) order below its Néel temperature of 311 K [1]. At low temperature, as in other bcc metals, screw dislocations control the plastic deformation due to their high lattice friction [2–5]. These dislocations glide in the $\{110\}$ planes [2, 3, 6] and have a Burgers vector equal to the smallest periodicity vectors of the bcc crystal lattice, $1/2\langle 111 \rangle$. As $1/2\langle 111 \rangle$ is not a periodicity vector of the AF magnetic order, such dislocations should trail magnetic faults while gliding [7, 8]. But, except this magnetic fault, *ab initio* calculations have shown that magnetism has a limited impact on the core properties of this screw dislocation [7].

In addition to this $\langle 111 \rangle\{110\}$ slip system, some experiments [3, 4] in Cr have also reported activity of $\langle 100 \rangle\{110\}$ slip systems, *i.e.* dislocation gliding in the same $\{110\}$ planes but with a $\langle 100 \rangle$ Burgers vector. Reid and Gilbert [3] observed with TEM in pure Cr deformed at 300 K slip traces corresponding to cross-slip events. As intersections between the primary and the cross-slipped $\{110\}$ planes were

along $\langle 100 \rangle$ and not $\langle 111 \rangle$ directions, this clearly indicate slip activity of $\langle 100 \rangle$ dislocations in bcc Cr, with an ability to cross-slip at ambient temperature. Existence of these $\langle 100 \rangle$ dislocations was later confirmed by Hale and Henderson Brown [4] who determined Burgers vectors through extinction experiments in TEM ($\vec{g}\cdot\vec{b}$ contrast). Although these $\langle 100 \rangle$ dislocations have a larger Burgers vector than $1/2\langle 111 \rangle$ dislocations, both have close core and elastic energy [7, 9]. The latter is a consequence of the strong elastic anisotropy of bcc Cr: with an anisotropy ratio $A = C_{44}/(C_{11} - C_{12})$ smaller than 1 ($A \simeq 0.68$), $\langle 100 \rangle$ screw dislocations have actually a lower elastic energy than $1/2\langle 111 \rangle$ ones in chromium [9]. Looking at their energy, there is thus no physical argument to discard *a priori* $\langle 100 \rangle$ dislocations. Besides, $\langle 100 \rangle$ dislocations do not disrupt the AF magnetic order and thus do not create magnetic fault in bcc Cr at low temperature, giving an additional reason to consider them.

$\langle 100 \rangle$ dislocations in bcc metals are the junction product resulting from the interaction of two $1/2\langle 111 \rangle$ dislocations, a reaction driven by elasticity [10]. Such a junction has been observed recently by transmission electron microscopy in Cr by Holzer *et al.* [5] on compressed single crystals at a temperature of 77 K. However, these authors did not report any activity of the $\langle 100 \rangle\{110\}$ slip system for the different orientations of the compression axis they

*Corresponding author

Email address: emmanuel.clouet@cea.fr (Emmanuel Clouet)

investigated. On the other hand, *ab initio* calculations have shown that these $\langle 100 \rangle$ screw dislocations have a Peierls energy barrier and a Peierls stress which are comparable to $1/2\langle 111 \rangle$ screw dislocations [7]. One would thus expect the coexistence of both dislocations in bcc Cr.

But plasticity in bcc metals has some complexity which prevents discussing the competition between different slip systems solely on the basis of their Peierls stress. Indeed, as opposed to face-centered cubic metals, bcc metals deviate from the predictions of the Schmid law [11–13]. The experimental yield stress measured under uniaxial loading on single crystals exhibits an asymmetry with respect to the orientation of the loading axis, a phenomenon known as the twinning/antitwinning (T/AT) asymmetry. A tension/compression (T/C) asymmetry also exists, with a yield stress generally lower in tension than in compression for the same loading axis [11, 14]. Such departures from the Schmid law have been shown to result from the trajectory of the gliding dislocation which locally deviates from the $\{110\}$ plane [15] and from the variations along this trajectory of the dislocation relaxation volume [16]. With all corresponding quantities extracted from *ab initio* calculations, one can build a generalized yield criterion going beyond the Schmid law to take full account of the specificities of the bcc crystal [17].

The object of the present work is to develop such a generalized yield criterion at 0 K in bcc Cr by means of *ab initio* calculations. Both screw dislocations with $1/2\langle 111 \rangle$ and $\langle 100 \rangle$ Burgers vectors are studied in order to compare their ease to glide in $\{110\}$ planes as a function of the orientation of the loading axis. Both non-magnetic (NM) and AF magnetic phases of Cr are considered to get further insights on the impact of magnetism on plasticity. The Peierls potentials for both slip systems and screw dislocation core properties are first presented before studying the dependence of $\langle 111 \rangle\{110\}$ and $\langle 100 \rangle\{110\}$ slip systems activity with the orientation of a uniaxial mechanical loading.

2. Computational details and methods

2.1. *Ab initio* parameters

All calculations have been performed within density functional theory (DFT) as implemented in the VASP code [18], using the same parameters as in our previous work [7]. A projector augmented wave

pseudopotential including 12 valence electrons is used to model Cr, with the GGA-PBE functional [19] to approximate the exchange and correlation potential. A plane-wave basis with an energy cutoff of 500 eV is used, with a Γ -centered k -point mesh generated using the Monkhorst-Pack scheme and sampling the Brillouin zone with 20 k -points per lattice parameter unit length in every direction. All atomic relaxations are performed in simulation cells with fixed periodicity vectors at the equilibrium lattice parameter and the stopping condition is set on the remaining forces on all atoms in every Cartesian directions to be below 5 meV/Å.

Magnetism is treated as collinear within spin-polarized DFT and spin-orbit coupling is not considered. As already thoroughly debated in various studies [7, 20–23], the spin-density wave (SDW) experimental magnetic ground-state of bcc Cr below its Néel temperature cannot be properly modeled using *ab initio* DFT calculations, which predicts the antiferromagnetic phase to have a lower energy than the SDW. The experimental SDW consists of a quasi-sinusoidal modulation of the magnetic moments of the atoms along a $\langle 100 \rangle$ axis of the crystal, with a locally AF order. However, as discussed in our previous work [7], the AF phase is a good approximate of the experimental SDW magnetic ground-state, with similar elastic properties and magnetic orders of the two phases.

Minimum energy paths between stable configurations are obtained with the nudged elastic band (NEB) method as implemented in VASP, with 5 intermediate images, and a spring constant of 5 eV/Å. The periodicity vectors of the supercell are kept fixed in these NEB calculations.

2.2. Simulation setup for dislocation modeling

A dislocation dipole is introduced in a periodic simulation cell using anisotropic elasticity theory, taking account of periodicity in all three Cartesian directions [24, 25]. To be able to extract precise dislocation positions and to obtain the Peierls stress via the derivative of the energy barrier with respect to the position, the simulation setup used in this study (Fig. 1 for the $1/2\langle 111 \rangle$ screw dislocation) is slightly different from the quadrupolar arrangement used in previous works [7, 15, 16].

In the quadrupolar arrangement which is usually preferred for modeling dislocation with periodic boundary conditions (positions indicated by blue dashed lines in Fig. 1), the two dipole dislocations contained in the simulation cell are sepa-

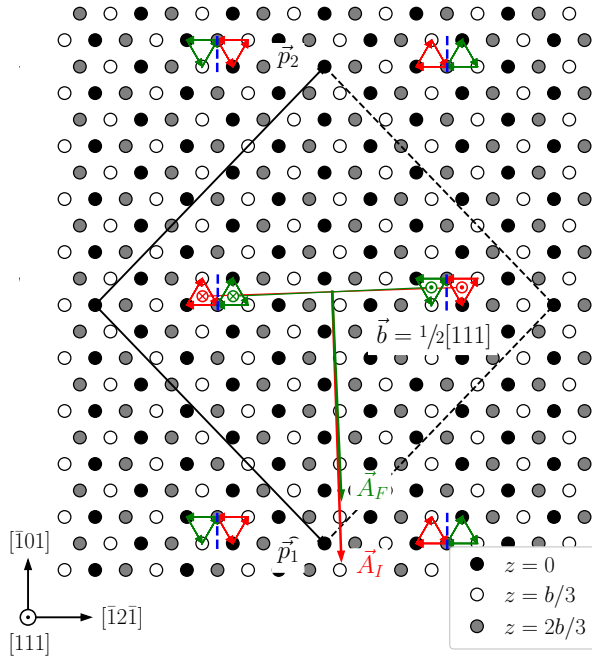


Figure 1: Dislocation setup used for the study of $1/2\langle 111 \rangle$ screw dislocations. Initial and final configurations of the NEB calculations are shown in red and green respectively. The position corresponding to a quadrupolar array is located at the intermediate position and is indicated by blue dashed lines.

rated by a vector $(\vec{p}_1 + \vec{p}_2)/2$, where \vec{p}_1 and \vec{p}_2 are the periodicity vectors of the simulation cell in the plane orthogonal to the dislocation line. This setup minimizes the elastic interactions between the dislocations and their periodic images. In the present setup, the two dislocations in their initial configuration are displaced from this quadrupolar position a distance equal to half the distance λ_P between two adjacent Peierls valleys, *i.e.* $+\lambda_P/2$ for $+\vec{b}$ dislocation and $-\lambda_P/2$ for $-\vec{b}$ (red configuration in Fig. 1). The final configuration (green configuration in Fig. 1) is obtained by displacing $+\vec{b}$ and $-\vec{b}$ by respectively $-\lambda_P$ and $+\lambda_P$ in their glide plane. Therefore, the position of the quadrupolar array lies half-way between the initial and final states of the NEB calculation. As a consequence, the variation of the elastic energy is symmetrical with respect to this quadrupolar position located in the middle of the path. In particular, the initial and final configurations are fully equivalent and have exactly the same elastic energy, as the distance between dislocations and their periodic images is the same in both configurations. To cancel the plastic strain generated by the dislocation dipole, a homogeneous

strain is applied to the periodicity vectors of the simulation cell [24, 25], which is calculated for the quadrupolar position located in-between the initial and final states. This choice preserves the symmetry of the path. Given that the dislocation setup is symmetrized with respect to the intermediate position, the displacements of the $+\vec{b}$ and $-\vec{b}$ screw dislocations are assumed to be identical in absolute value upon crossing the Peierls barrier. We checked the validity of this assumption by comparing atomic configurations of the two dislocation cores which were found to be fully equivalent in every image of the path for all the NEB calculations described below.

In addition to the Volterra elastic field, dislocations also induce a short-range dilatation field in the vicinity of their cores which can be modeled as an Eshelby inclusion defined by a relaxation volume tensor [16]. The dislocation positions and relaxation volume tensor can be evaluated from *ab initio* calculations taking advantage of the stress variation $\Delta\bar{\sigma}$ induced by moving dislocations in a simulation cell with fixed periodicity vectors [16, 17]. These variations are caused by changes in the distance between the two dislocations of the dipole, and by the variations of their relaxation volume. They are expressed as:

$$\Delta\sigma_{ij}(\xi) = \frac{C_{ijkl}}{hS} [b_k \Delta A_l(\xi) - 2h \Delta\Omega_{kl}(\xi)], \quad (1)$$

with ξ the reaction coordinate along the NEB path, \bar{C} the elastic constant tensor, \vec{b} the Burgers vector, S the surface of the simulation cell perpendicular to the dislocation line, of height h , and $\Delta\bar{\Omega}$ the variation of the dislocation relaxation volume tensor per unit length. $\Delta\vec{A}$ is the change in cut vector, indicated by red and green arrows in Fig. 1, and is related to the variation of the dislocation relative positions. Assuming that dislocations $+\vec{b}$ and $-\vec{b}$ are displaced from their initial positions by a vector $\vec{r}(\xi) = [x(\xi), y(\xi), 0]$ and $-\vec{r}(\xi)$, this variation of the cut vector is $\Delta\vec{A}(\xi) = 2h [y(\xi), -x(\xi), 0]$.

As extracted from the stress variation recorded along the NEB minimum energy path, the trajectories of the $1/2\langle 111 \rangle$ and $\langle 100 \rangle$ screw dislocations were not exactly located at the bottom of their Peierls valleys in the initial and final positions, and the relaxation volumes were not perfectly symmetrical with respect to the middle of the trajectory $\xi = 0.5$. To correct these small deviations, the elastic constants appearing in Eq. 1 were slightly adjusted. A variation of the components C_{15} and C_{44}

allows to recover the correct properties of the dislocation core and trajectory (Tab. A.3 and A.4). This does not appear disproportionate as the expression used to extract the dislocation trajectories and relaxation volumes is based on linear elasticity theory assuming that elastic constants are not perturbed by the presence of the dislocation dipole. As discussed in Appendix A, calculation of the elastic constants for a simulation cell containing the dislocation dipole show that such a variation of the elastic constants is reasonable and can be induced by anharmonicity. A similar correction was also reported to be necessary in tungsten [17].

Such NEB calculations, allowing for the determination of the dislocation position and of the relaxation volume along the minimum energy path, are performed in the following for the $1/2\langle 111 \rangle$ and $\langle 100 \rangle$ screw dislocations gliding in a $\{110\}$ plane in the NM and AF magnetic phases of bcc Cr.

3. Peierls potentials

3.1. $1/2\langle 111 \rangle$ screw dislocation

Periodicity vectors $(\vec{p}_1, \vec{p}_2, \vec{p}_3)$ of the simulation cell used for the study of the $1/2\langle 111 \rangle$ screw dislocation are given by $\vec{p}_1 = \lambda_1 \vec{u}_1 - \lambda_2 \vec{u}_2$, $\vec{p}_2 = \lambda_1 \vec{u}_1 + \lambda_2 \vec{u}_2$, and $\vec{p}_3 = n_3 \vec{u}_3$ (see Fig. 1). The glide plane of the dislocations is oriented by its normal $Y \parallel \vec{u}_2 = [\bar{1}01]$, the $X \parallel \vec{u}_1 = [\bar{1}2\bar{1}]$ axis is the glide direction, and the dislocation line is along the $Z \parallel \vec{u}_3 = 1/2[111]$ axis. The simulation cell contains 135 atoms per b in the Z direction, corresponding to $\lambda_1 = 5/2$ and $\lambda_2 = 9/2$. Periodicity vector \vec{p}_3 is defined by $n_3 = 1$ and 2 in the NM and AF phases respectively in order to respect the AF magnetic order in the $[111]$ direction.

In the following subsections, we first present results for the NM magnetic phase, and then for the AF phase where the magnetic fault created by the $1/2[111]$ dislocation dipole needs special care.

3.1.1. Non-magnetic phase

The Peierls energy barrier of the $1/2[111]$ screw dislocation gliding in the $(\bar{1}01)$ plane from the initial to final positions (red to green configuration of Fig. 1) is presented in Fig. 2. The barrier $\Delta E(\xi)$ obtained by NEB calculation needs to be corrected from the variation in elastic energy caused by the change in the distance between the two dislocations of the dipole along the path. This process is illustrated in Fig. 2 for the NM magnetic phase.

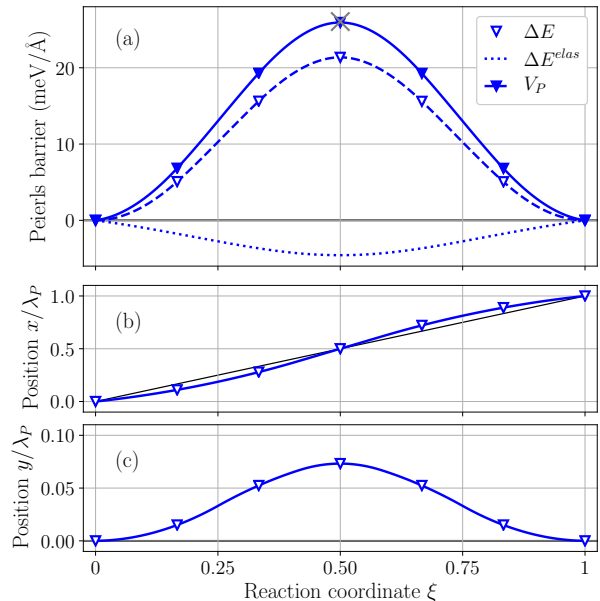


Figure 2: (a) NEB energy barrier ΔE (dashed line), variation of the elastic energy ΔE^{elas} (dotted line), and corrected Peierls potential V_P (solid line) for a $1/2\langle 111 \rangle$ screw dislocation gliding in a $\{110\}$ plane in the NM phase as a function of the reaction coordinate ξ . The height of the Peierls barrier previously obtained [7] with a setup without variation of the elastic energy is shown with a grey cross. (b) and (c) show the position of the screw dislocation projected along the X and Y axis respectively.

Using the position (x, y) (Fig. 2.b and c) of the dislocations deduced from the stress variation along the NEB path, the variation of the elastic energy of the dipole is evaluated using anisotropic elasticity theory [25]. This variation ΔE^{elas} of the elastic energy (dotted line in Fig. 2.a) is symmetrical with respect to the saddle point, as expected from the setup used in our simulations, and accounts for about one fifth of the energy variation observed in the NEB calculation. The energy variation ΔE recorded along the NEB calculation (dashed line) is then corrected from this variation of the elastic energy to obtain the Peierls potential V_P (solid line). For comparison, the height of the barrier obtained in our previous work using a dislocation setup where both dislocations glided in the same direction, thus without any variation of elastic energy, is indicated by a grey cross at $\xi = 0.5$. A very good agreement between the two setups is found, illustrating the correctness of the elastic energy calculation and the ability of this approach to lead to the Peierls potential despite the variations of the elastic energy along the path. One bene-

fit of these NEB calculations is that they allowed the determination of dislocation position along the energy barrier. Fig. 2 shows that the position x of the dislocation in its glide plane slightly differs from a simple proportionality relation, $x = \xi\lambda_P$, with the reaction coordinate ξ . Most importantly, with $y > 0$, the trajectory deviates from a straight line, a feature responsible for non-Schmid effects in bcc metals [15].

3.1.2. Antiferromagnetic phase

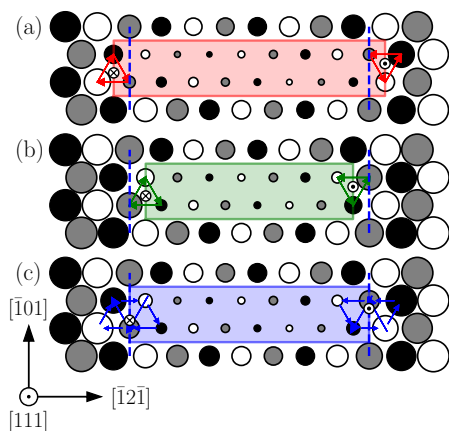


Figure 3: Differential displacement maps of the dislocation dipole in the AF magnetic phase with a fault located in the $(\bar{1}01)$ plane, in the (a) initial and (b) final configurations for the setup shown in Fig. 1. The colored rectangles indicate the range of the magnetic fault separating the two dislocations. The saddle configuration is shown in (c), located at the intermediate position. Atoms located at different heights along the $[111]$ direction are represented in different colors, and their diameters are proportional to their magnetic moments.

The disruption of the AF magnetic order by $1/2\langle 111 \rangle$ dislocations generates a magnetic fault separating the two dislocations composing the dipole [7]. Due to this fault, the energy of the initial and final configurations of the NEB path are not identical, leading to a negative slope on the energy barrier (curve $I \rightarrow F$ in Fig. 4) as the dislocations erase part of the magnetic fault when gliding (Fig. 3). With an energy of the magnetic fault $\gamma = 16.3 \text{ meV}/\text{\AA}^2$ [7], one expects an energy variation $\Delta E^{mag} = \lambda_P \gamma = 38.1 \text{ meV}/\text{\AA}$ per unit-length of dislocation. *Ab initio* calculations lead to an energy difference in good agreement (Fig. 4a), which is only slightly lower probably because of the perturbation of the magnetic fault by the dislocation core. To remove this magnetic contribution to the

energy barrier, we consider the same NEB calculation but read in the reverse direction. In this reversed path $F \rightarrow I$, the dislocations increase the width of the magnetic fault when gliding, now leading to a positive slope on the energy barrier (curve $F \rightarrow I$ in Fig. 4). Because of the symmetry of the bcc lattice and of our simulation setup where the quadrupolar position is centered in the middle of the path, the two paths $I \rightarrow F$ and $F \rightarrow I$ lead to the same variations of the Peierls and elastic energies. The average of the two energy barriers, $[\Delta E(\xi) + \Delta E(1 - \xi)]/2$, therefore cancels the magnetic contribution while keeping unchanged all other energy contributions. The same symmetrization procedure is applied to the stress variations to obtain the dislocation position and the variation of the relaxation volume along the path. The variation of the elastic energy is then removed to obtain the Peierls potential of the screw dislocation (Fig. 4) using the same procedure as for the NM phase. Once again, a perfect agreement is found concerning the height of the Peierls energy barrier between the present NEB calculations and previous ones [7] where the distance between dislocations was kept constant along the path (compare red solid line with grey cross in Fig. 4b).

3.1.3. Trajectory and relaxation volume

We now compare the trajectory of the $1/2\langle 111 \rangle$ screw dislocation when gliding in a $\{110\}$ plane obtained in the NM and AF magnetic phases as well as the variation of its relaxation volume (Fig. 5). As previously reported for all other bcc transition metals [15], the $1/2\langle 111 \rangle$ screw dislocation does not have a straight trajectory from one Peierls valley to the next nearest while gliding in a $\{110\}$ plane. The screw dislocation leaves its $\{110\}$ average macroscopic glide plane to move towards the split core configuration [26]. This can be described by a deviation angle α , defined by the tangent to the dislocation trajectory at the position corresponding to the maximum slope of the Peierls potential $V_P(x)$. This deviation angle α in bcc Cr is -13.5° and -7.0° in the NM and AF magnetic phases respectively. The deviation from a straight line of the dislocation trajectory is therefore more pronounced in the NM than in the AF magnetic phase, and one expects that the T/AT asymmetry will be more important in this NM phase.

In the frame of the simulation cell, the relaxation volume tensor of the gliding $1/2\langle 111 \rangle$ screw dislo-

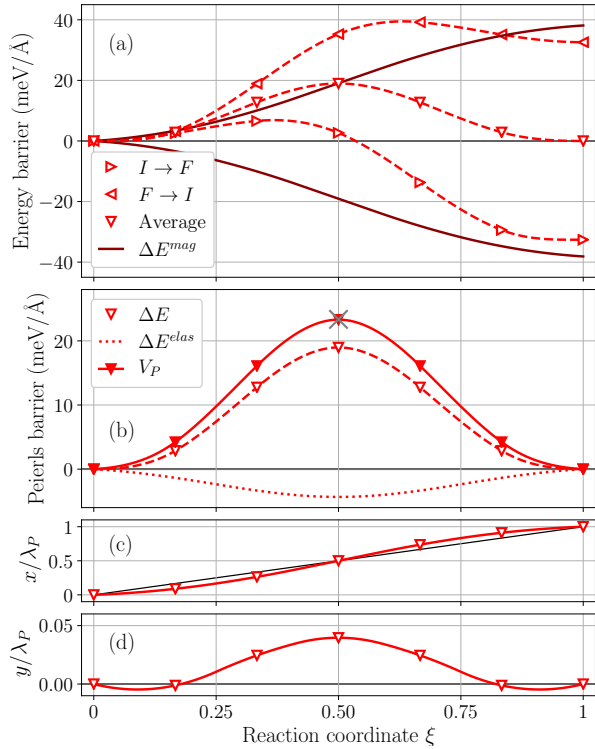


Figure 4: (a) Energy barriers following the two paths $I \rightarrow F$ and $F \rightarrow I$, with the variation of magnetic fault energy ΔE^{mag} for a $1/2\langle 111 \rangle$ screw dislocation gliding in a $\{110\}$ plane in the AF magnetic phase of bcc Cr as a function of the reaction coordinate ξ . (b) Peierls potential V_P obtained after averaging the paths $I \rightarrow F$ and $F \rightarrow I$. The height of the barrier obtained previously [7] is shown with a grey cross. (c) and (d) show the position of the dislocation along the X and Y axis respectively.

cation has the following form [16]:

$$\bar{\Omega}_{1/2\langle 111 \rangle} = \begin{bmatrix} \Omega_{11} & \Omega_{12} & 0 \\ \Omega_{12} & \Omega_{22} & 0 \\ 0 & 0 & \Omega_{33} \end{bmatrix}, \quad (2)$$

where Ω_{32} and Ω_{13} are negligible compared to the other components of the tensor. There is no symmetry argument imposing that these components should be null but, as also reported in the case of bcc tungsten [16, 17], post-processing of the $I \rightarrow F$ and $F \rightarrow I$ show that this is the case in Cr for both NM and AF magnetic phases. The variations of the relaxation volume tensor are extracted from the stress variation along the dislocation minimum energy path using Eq. 1 and by adjusting the elastic constants as introduced in section 2.2. The results are presented in Fig. 5.b as a function of the dislocation position.

As also reported in tungsten, the dilatation field

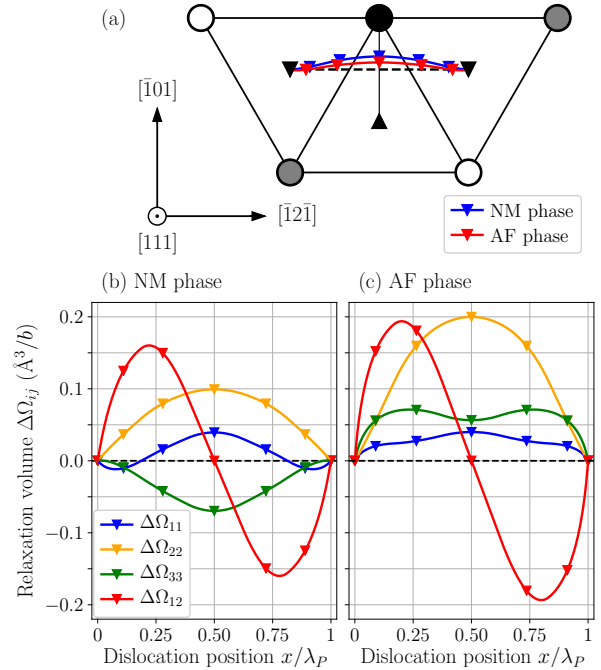


Figure 5: (a) Trajectory of a $1/2\langle 111 \rangle$ screw dislocation gliding in a $\{110\}$ plane in the NM (blue) and AF (red) phases. The variation of the relaxation volume tensor $\Delta\Omega_{ij}$ of the $1/2\langle 111 \rangle$ screw dislocation is presented for (b) the NM and (c) AF magnetic phases as a function of the dislocation position. The symbols are *ab initio* data after post-processing and lines are quadratic splines.

induced by the $1/2\langle 111 \rangle$ screw dislocation core does not remain isotropic upon crossing of the Peierls barrier. The shape of the dilatation field is defined by its ellipticity $\Delta\Omega_e = \Delta\Omega_{22} - \Delta\Omega_{11}$, which is higher in the AF than in the NM magnetic phase, and the tilt of the core deformation, $\Delta\Omega_t = 2\Delta\Omega_{12}$, which is similar in both phases. One therefore expects that the tension/compression asymmetry will be more important in the AF than in the NM phase. We note that the trace of the relaxation volume tensor is not zero, and also differs from one magnetic phase to the other. This induces a coupling between the dislocation core and the pressure. As a consequence, the yield stress will become sensitive to the applied pressure.

3.2. $\langle 100 \rangle$ screw dislocation

The simulation cell used for the $\langle 100 \rangle$ screw dislocations contains 200 atoms per b for both NM and AF magnetic phases, with periodicity vectors $\vec{p}_1 = 10 \times [100]$, $\vec{p}_2 = 10 \times [010]$, and $\vec{p}_3 = [001]$. Like for the $1/2\langle 111 \rangle$ screw dislocation (Fig. 1), the

quadrupolar position of the dislocation array is positioned in-between the two ground-state positions corresponding to the initial and final configurations of the NEB calculation. The crystal is oriented by the glide direction $X \parallel [110]$, the normal to the glide plane $Y \parallel [\bar{1}10]$, and the dislocation line $Z = [001]$. In this frame, the relaxation volume tensor of the $\langle 100 \rangle$ screw dislocation has the following form:

$$\bar{\bar{\Omega}}_{\langle 100 \rangle} = \begin{bmatrix} \Omega_{11} & 0 & 0 \\ 0 & \Omega_{22} & 0 \\ 0 & 0 & \Omega_{33} \end{bmatrix} \quad (3)$$

Like $1/2\langle 111 \rangle$ screw dislocations, post-processing of the stress variations along the two $I \rightarrow F$ and $F \rightarrow I$ paths show that Ω_{13} and Ω_{32} are zero for the $\langle 100 \rangle$ screw dislocation gliding in a $\{110\}$ plane. As for the Ω_{12} component, the mirror symmetry of the $\{110\}$ glide plane imposes its nullity. This is the case for both magnetic phases. As no magnetic fault is generated by $\langle 100 \rangle$ dislocations in the AF phase, the dislocation trajectory and the variation of its relaxation volume tensor can be directly extracted from the stress variation recorded along the NEB path between the initial and final configurations in both magnetic phases.

The Peierls energy barrier opposing $\langle 100 \rangle$ screw dislocation glide in a $\{110\}$ plane in the NM and AF magnetic phases is presented in Fig. 6.a and b in solid lines as a function of the reaction coordinate ξ after subtraction of the variation of the elastic energy. The heights of the barrier obtained in our previous work [7] with a setup where both dislocations glide in the same direction are represented by a grey cross at $\xi = 0.5$ for comparison. Very good agreement is found between the two setups concerning the Peierls potential of the $\langle 100 \rangle$ screw dislocation, proving once again the validity of the elastic correction.

The trajectory followed by the $\langle 100 \rangle$ screw dislocation along its minimum energy path when gliding in a $\{110\}$ plane is presented in Fig. 7.a in the NM and AF magnetic phases. For clarity, the trajectories have been shifted up and down. We note that the $\langle 100 \rangle$ screw dislocation follows a straight trajectory between two adjacent Peierls valleys in a $\{110\}$ plane, and is almost identical in both magnetic phases. This is also a consequence of the mirror symmetry of the $\{110\}$ glide plane. As the dislocation trajectory coincides with the macroscopic glide plane, $\langle 100 \rangle \{110\}$ slip systems should not show any T/AT asymmetry, unlike $\langle 111 \rangle \{110\}$ slip systems.

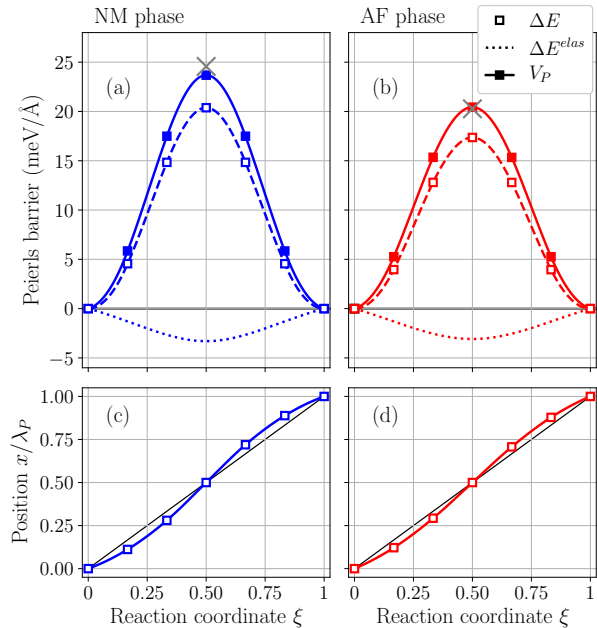


Figure 6: Peierls potential V_P (solid lines) of a $\langle 100 \rangle$ screw dislocation gliding in a $\{110\}$ plane in (a) the NM and (b) AF magnetic phases as a function of the reaction coordinate ξ . The position of the dislocation in the glide plane is shown in (c) and (d) in the NM and AF phases respectively.

Variations of the relaxation volume as a function of the dislocation position x are presented in Fig. 7.b and c in the NM and AF magnetic phases respectively. Although relaxation volume tensor remains diagonal, the high symmetry of the core dilatation field is broken along the path, with the development of an elliptic contribution $\Delta\Omega_{22} - \Delta\Omega_{11}$ and of a non-negligible trace. Yield stress of the $\langle 100 \rangle$ screw dislocation should therefore experience tension/compression asymmetry and be sensitive to the applied pressure. The variation of the relaxation volume tensor is similar in the NM and AF phases, except for $\Delta\Omega_{33}$ which is almost negligible in the AF phase.

3.3. Peierls stresses

The Peierls barriers obtained after correction of the elastic and magnetic fault contributions are presented in Fig. 8 as a function of the dislocation position x for both dislocations and magnetic phases. The Peierls stress τ_P necessary to overcome the energy barrier can be evaluated precisely using the dislocation position x extracted from NEB calculations. The Peierls stress is calculated from the

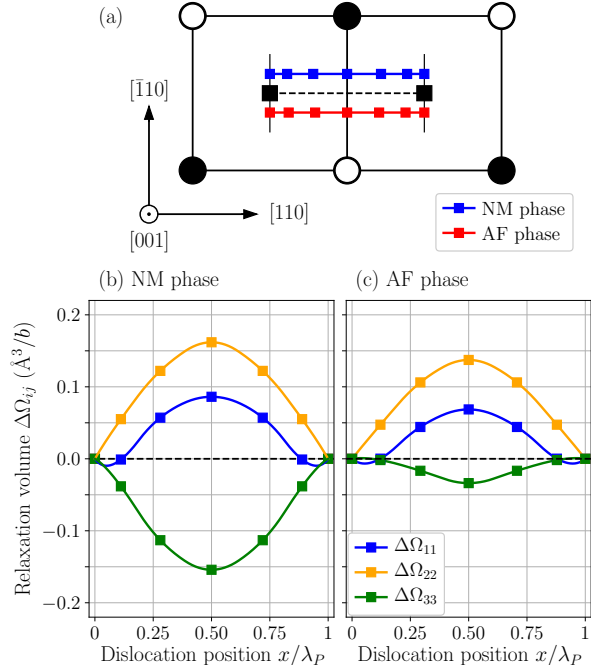


Figure 7: (a) Trajectory of a $\langle 100 \rangle$ screw dislocation gliding in a $\{110\}$ plane in the NM (blue) and AF (red) phases. The trajectories, which are straight and coincide with the black dashed line, have been shifted upwards (NM) and downwards (AF) for clarity. The variations of the relaxation volume tensor $\Delta\Omega_{ij}$ are presented for (b) the NM and (c) AF magnetic phases as a function of the dislocation position.

maximum slope of the Peierls potential:

$$\tau_P = \frac{1}{b} \max_x \left[\frac{\partial V_P(x)}{\partial x} \right], \quad (4)$$

with b the norm of the considered Burgers vector, namely $a_0\sqrt{3}/2$ and a_0 for $1/2\langle 111 \rangle$ and $\langle 100 \rangle$ screw dislocations respectively. We obtain a Peierls stress of 2.3 and 2.0 GPa for the $1/2\langle 111 \rangle$ screw dislocation gliding in a $\{110\}$ plane in the NM and AF magnetic phases respectively. The Peierls stress of the $\langle 100 \rangle$ screw dislocation gliding in a $\{110\}$ plane is 2.2 and 1.7 GPa in the NM and AF phases respectively. For both screw dislocations and both magnetic phases, the Peierls stress does not deviate by more than 0.1 GPa from the value obtained in our previous work [7] where the dislocation position x was assumed to vary linearly with the reaction coordinate ξ . Trajectories extracted from the NEB calculations with the present setup (Figs. 2b, 4c and 6c and d) show that it was indeed a reasonable assumption. These new NEB calculations confirm that the Peierls stresses of the $1/2\langle 111 \rangle$ and $\langle 100 \rangle$ screw dislocations are comparable in both

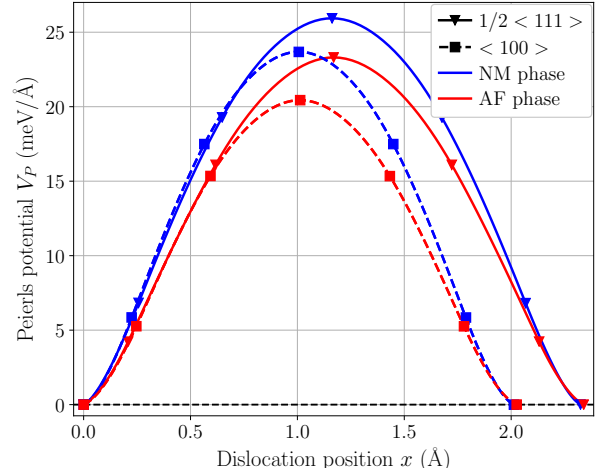


Figure 8: Peierls potential V_P for $1/2\langle 111 \rangle$ (solid lines) and $\langle 100 \rangle$ (dashed lines) screw dislocations gliding in a $\{110\}$ plane in the NM (blue) and AF (red) magnetic phases of bcc Cr as a function of the dislocation position x .

magnetic phases, and that the two $\langle 111 \rangle\{110\}$ and $\langle 100 \rangle\{110\}$ slip systems should be competitive on the basis of their mobilities. However, as we now know precisely the trajectory followed by the dislocation along its minimum energy path when gliding in a $\{110\}$ plane and also the variations of its relaxation volume along this path, it becomes possible to study in more details the competition between these two slip systems, taking full account of non-Schmid effects.

4. Slip activity

In this section, the dependence of the yield stress for $\langle 111 \rangle\{110\}$ and $\langle 100 \rangle\{110\}$ slip systems is studied as a function of the orientation of the loading axis taking non-Schmid effects into account.

4.1. Yield stress

The application of a stress tensor $\bar{\Sigma}$ on a gliding dislocation results in a change in its enthalpy ΔH_P per unit length as it crosses the Peierls barrier given by:

$$\Delta H_P^{2D}(x, y) = V_P^{2D}(x, y) + \Sigma_{ij} b_i \Delta A_j(x, y) - \Sigma_{ij} \Delta \Omega_{ij}^{2D}(x, y), \quad (5)$$

where (x, y) is the position of the dislocation in the $\{111\}$ plane, V_P^{2D} is the 2D Peierls potential, defining the dislocation enthalpy ΔH_P as a 2D function of the dislocation position. By assuming that the

trajectory of the dislocation between two adjacent Peierls valleys is not sensitive to the mechanical loading, which has been verified by *ab initio* calculations for tungsten [16, 17], it is possible to define ΔH_P as a 1D functional of the dislocation position x :

$$\begin{aligned}\Delta H_P^{1D}(x) &= \Delta H_P^{2D}(x, \bar{y}(x)) \\ &= V_P^{1D}(x) + \Sigma_{ij} b_i \Delta A_j(x) \\ &\quad - \Sigma_{ij} \Delta \Omega_{ij}^{1D}(x),\end{aligned}\quad (6)$$

where $\Delta \vec{A}(x) = 2h [\bar{y}(x), -x, 0]$, $\bar{y}(x)$ is the dislocation trajectory and $\Delta \bar{\Omega}^{1D}(x)$ is the variation of the relaxation volume along the NEB minimum energy path. The second term in the right hand side of Eq. 6 is the work of the Peach-Koehler force acting on the gliding dislocation, resulting from the coupling between the dislocation trajectory and the applied stress, and the last term describes the coupling between the dislocation relaxation volume and non-glide components of the applied stress.

The yield stress σ_Y necessary to overcome the Peierls barrier is found at the unstable position x^* satisfying the following conditions:

$$\left. \frac{\partial \Delta H_P^{1D}}{\partial x} \right|_{x^*} = 0 \quad \text{and} \quad \left. \frac{\partial^2 \Delta H_P^{1D}}{\partial x^2} \right|_{x^*} = 0, \quad (7)$$

corresponding to the inflexion point of the Peierls enthalpy barrier ΔH_P as a function of the dislocation position x . In the following, this method is applied to the case of uniaxial loading. However more complex loadings can be considered following the same scheme by changing the considered stress tensor in Eq. 6.

4.2. Uniaxial loading

Under uniaxial loading of magnitude σ along an axis \vec{t} , the stress tensor is:

$$\bar{\Sigma} = \sigma(\vec{t} \otimes \vec{t}) \quad (8)$$

By expressing the tensile axis in the frame of the gliding dislocation, the above stress tensor is given by:

$$\sigma \begin{bmatrix} \sin^2 \zeta \sin^2 \chi & 1/2 \sin^2 \zeta \sin 2\chi & 1/2 \sin 2\zeta \sin \chi \\ & \sin^2 \zeta \cos^2 \chi & 1/2 \sin 2\zeta \cos \chi \\ & & \cos^2 \zeta \end{bmatrix}, \quad (9)$$

where ζ is the angle between the slip direction (or Burgers vector \vec{b}) of the gliding dislocation and the tensile axis \vec{t} , and χ is the angle between the normal \vec{n} to the glide plane and the plane of maximum

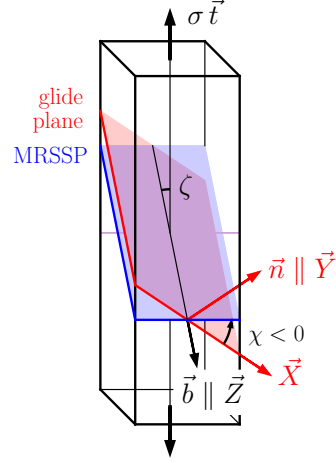


Figure 9: Schematic representation of a single crystal under uniaxial loading along the axis \vec{t} , showing the dislocation glide plane of normal \vec{n} , the slip direction b , the glide direction \vec{X} and the MRSSP defining the angles ζ and χ .

resolved shear stress (MRSSP). A sketch of the sample under uniaxial loading, with the angles ζ and χ is shown in Fig. 9.

To have a physical understanding of the contribution of the relaxation volumes to the yield stress, it is helpful to define the following quantities:

$$\begin{aligned}\Delta \Omega_P &= \text{Tr} \Delta \bar{\Omega} = \Delta \Omega_{11} + \Delta \Omega_{22} + \Delta \Omega_{33} \\ \Delta \Omega_e &= \Delta \Omega_{22} - \Delta \Omega_{11} \\ \Delta \Omega_t &= 2\Delta \Omega_{12}\end{aligned}\quad (10)$$

where $\Delta \Omega_P$ represents the coupling with pressure, $\Delta \Omega_e$ is the ellipticity of the dislocation core field, and $\Delta \Omega_t$ is the transverse variation. In the case of uniaxial loading, the dislocation enthalpy ΔH_P^{1D} of Eq. 6 per unit length can be written as:

$$\begin{aligned}\Delta H_P^{1D}(x) &= V_P^{1D}(x) \\ &\quad - \frac{1}{2} \sigma b \sin(2\zeta) [-y(x) \sin \chi + x \cos \chi] \\ &\quad - \frac{1}{2} \sigma \sin^2 \zeta [\Delta \Omega_P(x) + \Delta \Omega_e(x) \cos(2\chi) \\ &\quad \quad + \Delta \Omega_t(x) \sin(2\chi)] \\ &\quad + \frac{1}{2} \sigma (1 - 3 \cos^2 \zeta) \Delta \Omega_{33}(x)\end{aligned}\quad (11)$$

Taking the first and second derivatives of the above enthalpy at the inflexion point x^* and applying the conditions of Eq. 7 gives the following expression for the yield stress in tension:

$$\sigma_Y(\zeta, \chi) = \frac{2\tau_P}{\sin(2\zeta) \frac{\cos(\chi - \alpha)}{\cos(\alpha)} + \beta(\zeta, \chi)}, \quad (12)$$

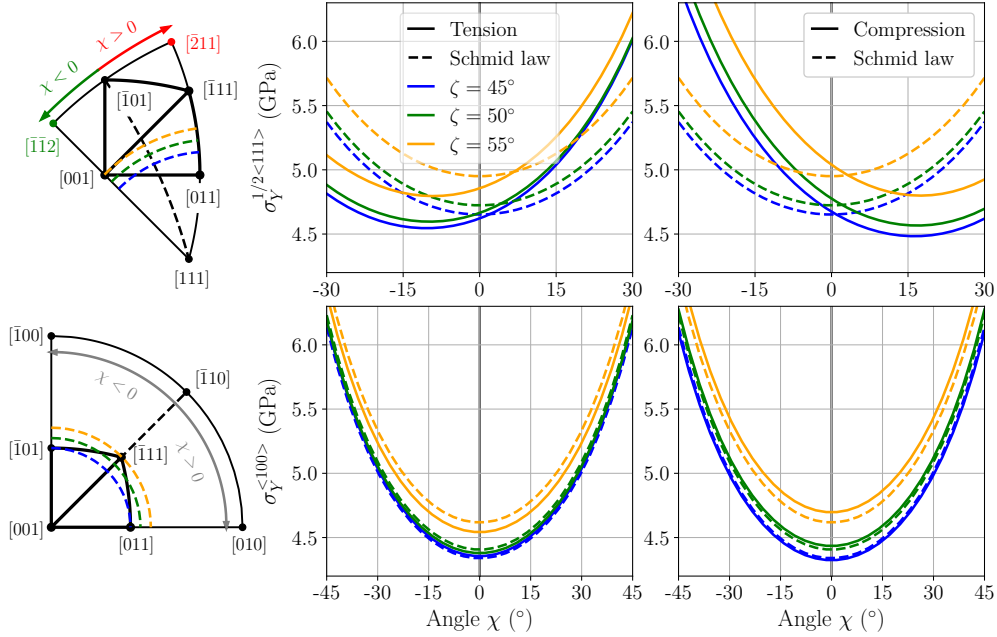


Figure 10: Yield stress σ_Y predicted by the criterion of Eq. 12 for $[111](\bar{1}01)$ (first row) and $[001](\bar{1}10)$ (second row) slip systems under uniaxial loading as a function of the angle χ at constant $\zeta = 45^\circ, 50^\circ, 55^\circ$ lines in the NM magnetic phase. Results are shown according to the Schmid law and including non-Schmid effects in tension, and compression. The stereographic projection corresponding to each slip system is shown in the first column.

where β is a function of the angles ζ and χ which incorporates all the contributions of the core dilatation. It only depends on the derivatives of the relaxation volumes with respect to the position x at the inflexion point:

$$\beta(\zeta, \chi) = \sin^2 \zeta \left[\frac{\Delta \Omega'_e}{b} \cos(2\chi) + \frac{\Delta \Omega'_t}{b} \sin(2\chi) + \frac{\Delta \Omega'_P}{b} \right] - (1 - 3 \cos^2 \zeta) \frac{\Delta \Omega'_{33}}{b} \quad (13)$$

The superscripts ' and * denote the first derivative with respect to x and its value at the inflexion point x^* respectively. The yield stress in compression is found by applying Eq. 7 at the mirror-symmetry equivalent of the inflexion point x^* , located at $\lambda_P - x^*$. The yield stress has the same form as in tension but the parameters of the criterion have different signs according to the derivatives of the relaxation volumes at this symmetrical position. The parameters of the above criterion for both $1/2\langle 111 \rangle$ and $\langle 100 \rangle$ screw dislocations gliding in a $\{110\}$ in the NM and AF magnetic phases of bcc Cr are given in Tab. 1. We checked that this analytical expression gives a quantitative description of the yield stress for all orientations of the tensile

axis by comparing with the numerical resolution of Eq. 7.

An analytical expression for a similar yield criterion was introduced by Vitek and co-workers [27–30], with a different form than the one presented here. The main reason for these two formulations is that the mechanical loadings considered are different. In the work of Vitek *et al.*, the mechanical loading is a superposition of a shear stress τ in the MRSSP, and a tensile/compressive stress σ normal to the MRSSP, leading to:

$$\begin{bmatrix} -\sigma \cos(2\chi) & -\sigma \sin(2\chi) & \tau \sin \chi \\ & \sigma \cos(2\chi) & -\tau \cos \chi \\ & & 0 \end{bmatrix}, \quad (14)$$

where the two stress components τ and σ are independent. Using this stress tensor in Eq. 6, Kraych *et al.* have shown that the yield criterion of Vitek *et al.* is recovered (see supplementary materials of Ref. [16]), if the components $\Delta \Omega_P$ and $\Delta \Omega_{33}$ of the dislocation relaxation volume can be neglected.

When non-Schmid effects are neglected, *i.e.* the dislocation trajectory is assumed to be straight between two adjacent Peierls valleys and the relaxation volume of the dislocation core does not vary along the path, the dislocation enthalpy of Eq. 11

is:

$$\Delta H_P^{1D}(x) = V_P^{1D}(x) - \frac{1}{2}\sigma b x \sin(2\zeta) \cos(\chi), \quad (15)$$

where $\text{SF}(\zeta, \chi) = \sin(2\zeta) \cos(\chi)/2$ is the Schmid factor of the slip system. Applying the conditions of Eq. 7 to this simplified enthalpy gives the following expression for the yield stress:

$$\sigma_Y(\zeta, \chi) = \frac{2\tau_P}{\sin(2\zeta) \cos(\chi)} = \frac{\tau_P}{\text{SF}(\zeta, \chi)}, \quad (16)$$

resulting in the Schmid law, which can be retrieved from Eq. 12 taking $\alpha = 0$ and $\beta(\zeta, \chi) = 0$. The variation of the predicted yield stress σ_Y as a function of the angle χ at a constant ζ is presented in Fig. 10 for $[111](\bar{1}01)$ and $[001](\bar{1}10)$ slip systems in the first and second rows respectively, considering the NM magnetic phase. The T/AT asymmetry of $\langle 111 \rangle \{110\}$ slip is clearly seen, showing an easier glide in the $\chi < 0$ region in tension, and the opposite in compression. Apart from the easier twinning sense, the asymmetry between tensile and compressive behaviors is small, with a slightly lower yield stress in tension in the center of the standard stereographic triangle. As for the $[001](\bar{1}10)$ system, no asymmetry between twinning and antitwinning is found, as was expected from the straight trajectory of the $\langle 100 \rangle$ screw dislocation in $\{110\}$ planes, and the tensile and compressive yield stresses are also comparable.

The predicted yield stress in the AF phase shows the same qualitative features as in the NM phase (see Fig. 1 in Supplementary Materials). Quantitatively, a lower yield stress is found for both slip systems, due to the lower Peierls stresses τ_P in the AF phase, and the T/AT asymmetry of $\langle 111 \rangle \{110\}$ slip is less pronounced than in the NM phase, because of the lower deviation α . However, tension/compression asymmetry for $\langle 111 \rangle \{110\}$ is more pronounced given the higher magnitude of the relaxation volumes in the AF phase, and is almost identical to the NM case for $\langle 100 \rangle \{110\}$ (Tab. 1).

In the following section, we use the obtained yield criterion to consider the competition between the different $\langle 111 \rangle \{110\}$ and $\langle 100 \rangle \{110\}$ slip systems for all possible orientations of the tensile/compressive axis at 0 K in the NM and AF magnetic phases of bcc Cr.

Table 1: Parameters of the yield criterion of Eq. 12 for $\langle 111 \rangle \{110\}$ and $\langle 100 \rangle \{110\}$ slip systems in the NM and AF magnetic phases of bcc Cr under uniaxial loading: Peierls stress τ_P (GPa), angle α ($^\circ$), and derivatives of the relaxation volumes with respect to the dislocation position x at the inflexion point x^* . The signs of the parameters correspond to tension/compression values.

	$\langle 111 \rangle \{110\}$		$\langle 100 \rangle \{110\}$	
	NM	AF	NM	AF
τ_P	± 2.32	± 1.98	± 2.17	± 1.74
α	∓ 13.46	∓ 6.970	0	0
$\Delta \Omega_P^*$	± 0.041	± 0.171	± 0.058	± 0.099
$\Delta \Omega_e^*$	± 0.025	± 0.103	± 0.007	± 0.015
$\Delta \Omega_t^*$	$+0.133$	$+0.237$	0	0
$\Delta \Omega_{33}^*$	∓ 0.034	± 0.041	∓ 0.086	∓ 0.014

4.3. Competition between $1/2\langle 111 \rangle$ and $\langle 100 \rangle$

Using the yield criterion of Eq. 12, the yield stress σ_Y of all slip systems of the $\langle 111 \rangle \{110\}$ and $\langle 100 \rangle \{110\}$ types is evaluated as a function of the orientation of the tensile axis in the region of the stereographic projection shown in the upper row of Fig. 10. This region encapsulates the whole range of orientations to characterize the plastic anisotropy of both slip systems. The results for the NM phase are presented in the first row of Fig. 11 according to the Schmid law, and including non-Schmid effects in tension and compression. The distribution of primary slip systems predicted by the Schmid law is a direct image of the ratio between the Peierls stresses of $1/2\langle 111 \rangle$ and $\langle 100 \rangle$ screw dislocations, weighted by their respective Schmid factors. The regions colored in green represent the range of loading orientations where a $\langle 100 \rangle \{110\}$ system requires a lower stress to operate than a $\langle 111 \rangle \{110\}$ system. These regions are close to a $\langle 111 \rangle$ axis, where the maximum Schmid factor of a $\langle 111 \rangle \{110\}$ system is below 0.3 whereas it concentrates the orientations for which the Schmid factor of a $\langle 100 \rangle \{110\}$ is maximum. According to these results, $\langle 100 \rangle$ slip should be observed for a large range of loading orientations in both tension and compression.

The distribution of the corresponding primary slip systems in the NM phase, *i.e.* with the lowest yield stress at a given loading orientation, is shown on the second row of Fig. 11. If $\langle 100 \rangle \{110\}$ systems were not considered, the Schmid law predicts a single $\langle 111 \rangle \{110\}$ primary slip system in each of the $\langle 100 \rangle - \langle 110 \rangle - \langle 111 \rangle$ triangle, and the repartition of the yield stress would follow its Schmid factor in each triangle. With non-Schmid effects,

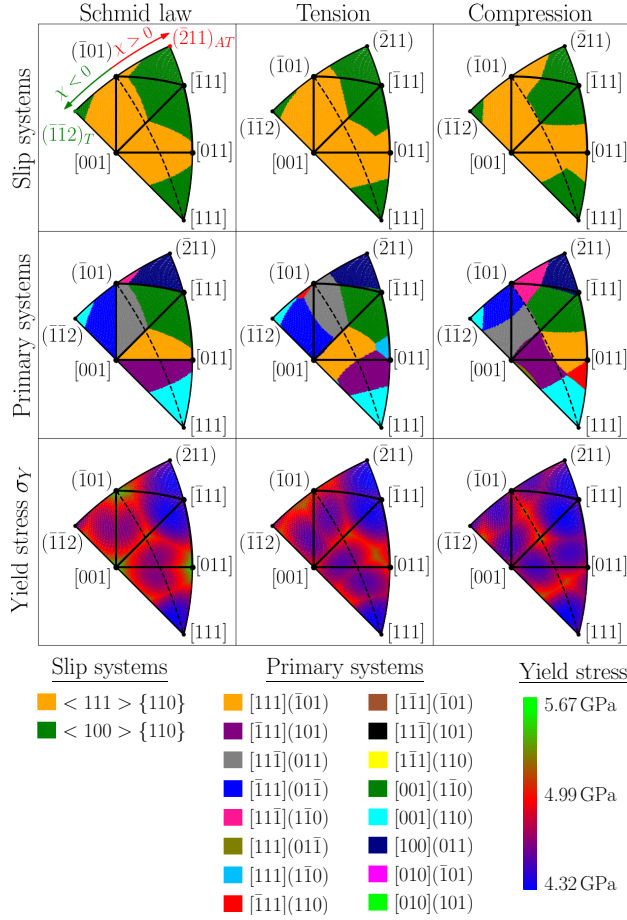


Figure 11: Type of slip systems (first row), with the corresponding primary system (second row) and yield stress σ_Y (third row) for bcc Cr in the NM magnetic phase under uniaxial loading, both according to the Schmid law (first column), and including non-Schmid effects in tension (second column), and compression (third column).

the orientations resulting in the lowest yield stress to activate a given $\langle 111 \rangle \{110\}$ system are shifted towards $\chi < 0$ in tension, and $\chi > 0$ in compression as a consequence of the T/AT asymmetry due to the deviated trajectory of the $1/2\langle 111 \rangle$ screw dislocation. As this affects every slip system of this family, we see the appearance of a region where $[\bar{1}\bar{1}1](101)$ (purple) is easier to activate in compression near $[001]$, and $[111](\bar{1}10)$ in tension (sky blue) near the $[011] - [\bar{1}\bar{1}1]$ edge of the standard stereographic triangle. We also note that the maximum Schmid factor among $\langle 100 \rangle \{110\}$ systems goes to zero for loading axis close to the $[001]$ corner of the stereographic triangle. When non-Schmid effects are taken into account, the region where $\langle 100 \rangle \{110\}$ slip systems are easier to activate is reduced in compression as

$[111](\bar{1}01)$ glides more easily in the $\chi > 0$ zone.

The results in the AF magnetic phase show the same qualitative features as in the NM phase (see Fig. 2 in Supplementary Materials). However, as the ratio $\tau_P^{(100)}/\tau_P^{1/2\langle 111 \rangle}$ between Peierls stresses is slightly lower than in the NM phase (0.89 and 0.94 respectively, see Tab. 1), a larger range of loading orientations favors $\langle 100 \rangle \{110\}$ slip over $\langle 111 \rangle \{110\}$.

5. Discussion

5.1. Deviation from the Schmid law

Looking separately to the dislocations with two possible Burgers vectors, the $\langle 111 \rangle \{110\}$ slip systems show a behavior deviating noticeably from the predictions of the Schmid law. The main experimental features of plasticity in bcc metals are well captured by the model, namely the T/AT asymmetry and the asymmetrical behaviors in tension and compression with an overall lower yield stress in tension in the center of the stereographic triangle.

On the other side, $\langle 100 \rangle \{110\}$ slip systems do not show T/AT asymmetry since $\langle 100 \rangle$ screw dislocations have a straight trajectory in $\{110\}$ planes. Only the coupling of the dislocation relaxation volume with the applied stress has an effect on the predicted yield stress. For these $\langle 100 \rangle \{110\}$ slip systems, an almost negligible deviation from the Schmid law is predicted, as shown in the second row of Fig. 10.

Qualitatively, magnetism has only a small influence on the yield behavior of bcc Cr under uniaxial loading. Indeed, the deviation angle defining dislocation trajectory and T/AT asymmetry is almost the same in both magnetic phases and the relaxation volumes of the two screw dislocations also follow the same trends. However, the tension/compression asymmetry is more pronounced in the AF phase as a result of the higher magnitude of its components, whereas the T/AT asymmetry is more pronounced in the NM phase with a deviation angle twice the value found in the AF phase. As the Peierls stress of both screw dislocations is slightly lower in the AF than in the NM phase, the overall yield stress required to activate slip is lower. However, the predicted primary slip systems are the same in the two magnetic phases, covering a more or less equivalent space in the stereographic projection shown in Fig. 11.

5.2. Competing slip systems and comparison with experimental data

Observations of dislocations with a $\langle 100 \rangle$ Burgers vector have been reported in various experimental studies: in polycrystalline samples at room temperature by Hale and Henderson Brown [4] using a two-beam extinction criterion in transmission electron microscopy, by Reid and Gilbert [3] through a cross-slip event incompatible with a $1/2\langle 111 \rangle$ dislocation, and by both McLaren [2] and Garrod and Wain [31] in an annealed sample as part of hexagonal dislocation networks formed by intersecting $1/2\langle 111 \rangle$ dislocations. Holzer *et al.* [5] also report the presence of $\langle 100 \rangle$ dislocations in a compressed single-crystal at 77 K oriented at the center of the stereographic triangle, formed by the intersection of two $1/2\langle 111 \rangle$ screw dislocations.

Our *ab initio* modeling predicts $\langle 100 \rangle\{110\}$ slip to occur in a large portion of the standard stereographic triangle, mainly near $\langle 111 \rangle$ orientations (see Fig. 11) where slip systems having all three $\langle 100 \rangle$ Burgers vectors have the same Schmid factor. For instance, in the case of the $[\bar{5}911]$ single crystal tested in compression by Holzer *et al.* [5], strong $\langle 100 \rangle\{110\}$ slip activity is expected. The predicted yield stress for the slip systems having the 6 highest Schmid factors are presented in Tab. 2, among which the two most stressed are of the $\langle 100 \rangle\{110\}$ type. For this orientation, the authors report slip activity on both $(\bar{1}01)$ and $(\bar{1}10)$ planes through the rotation of the sample towards the corresponding poles of the stereographic projection. They attributed this observation to the activity of a $\langle 111 \rangle\{110\}$ slip system for both observed slip planes. However, according to our yield criterion, the lowest yield stress for a $\langle 111 \rangle\{110\}$ slip system in compression for $(\bar{1}10)$ slip is 6.95 GPa in the AF phase, whereas it is only 3.68 GPa for a $\langle 100 \rangle\{110\}$ system, suggesting slip might have occurred through the operation of the $[001](\bar{1}10)$ slip system. As for slip on $(\bar{1}01)$ plane, it is probably due to the operation of the highly stressed $[111](\bar{1}01)$ system, but can also be interpreted as the operation of the $[010](\bar{1}01)$ slip system, which has a lower predicted yield stress in compression.

The contribution of the different slip systems to the development of the plastic strain depends not only on the dislocation ease to glide but also on the corresponding dislocation density and their multiplication propensity. Hale and Henderson Brown [4] measured the ratio of presence between $1/2\langle 111 \rangle$, $\langle 100 \rangle$, and $\langle 110 \rangle$ dislocations in both iron (Fe) and

Table 2: Predicted yield stress for Cr single crystal under uniaxial compression along $[\bar{5}911]$ ($\zeta = 54.9^\circ, \chi = 23.4^\circ$) considering the AF magnetic phase.

Slip system	SF	Schmid law	Compression
$[111](\bar{1}01)$	0.432	4.59 GPa	4.45 GPa
$[111](\bar{1}10)$	0.378	5.25 GPa	6.95 GPa
$[\bar{1}11](101)$	0.270	7.35 GPa	8.18 GPa
$[001](\bar{1}10)$	0.480	3.62 GPa	3.68 GPa
$[010](\bar{1}01)$	0.449	3.87 GPa	3.98 GPa
$[100](011)$	0.312	5.58 GPa	5.25 GPa

Cr using TEM observations. For a single extinction criterion $\vec{g} \cdot \vec{b} = 0$, they reported a ratio of 60:20:20 for Fe, and 46:36:18 for Cr, thus leading to a non-negligible density of $\langle 100 \rangle$ dislocations compared to $1/2\langle 111 \rangle$, with a higher proportion in Cr than in Fe. This relative density of $\langle 100 \rangle$ dislocations is, nevertheless, probably overestimated because of the use of an extinction criterion with a single \vec{g} vector. Using at least two different \vec{g} vectors, the measured ratios in Fe were now 94:5:1, with thus a much lower, but still non-negligible, relative density of $\langle 100 \rangle$ dislocations. Unfortunately, no analysis with two extinction conditions was performed in Cr. One can only expect that a lower proportion of $\langle 100 \rangle$ dislocations would be obtained than with a single extinction condition, but that the relative density will still be relevant, like in Fe. These $\langle 100 \rangle$ dislocations are actually observed as junctions between intersecting $1/2\langle 111 \rangle$ dislocations [5]. At low temperature, 77 K in the work of Holzer *et al.* [5], all $\langle 100 \rangle$ and $1/2\langle 111 \rangle$ dislocations are lying along their screw orientation. Our *ab initio* results indicate that resolved shear stress necessary to activate glide of the $\langle 100 \rangle$ screw dislocations is lower than for the $1/2\langle 111 \rangle$. These junctions could therefore act as sources of $\langle 100 \rangle$ dislocations for well oriented mechanical loadings. This will allow for the increase of $\langle 100 \rangle$ dislocation density, unless another character has a higher Peierls stress than the screw orientation and impedes the activation of $\langle 100 \rangle$ sources.

6. Conclusion

Through *ab initio* evaluation of the Peierls barriers opposing $1/2\langle 111 \rangle$ and $\langle 100 \rangle$ screw dislocations glide in $\{110\}$ planes, a yield criterion incorporating non-Schmid effects has been proposed for bcc Cr and applied to uniaxial loading. Both the trajectory and variations of the relaxation volume of

the two screw dislocations have been taken into account. As in other bcc metals [15], the deviated trajectory of $1/2\langle 111 \rangle$ screw dislocations results in T/AT asymmetry. On the other hand, $\langle 100 \rangle$ screw dislocations have a straight trajectory from one Peierls valley to the next nearest in a $\{110\}$ plane. Hence the yield behavior of these slip systems do not show T/AT asymmetry. The asymmetry between tensile and compressive behaviors arises from the coupling between the applied stress and the variations of the relaxation volume of the dislocation core field, resulting in a generally lower yield stress in tension than in compression.

A compact form of the yield criterion for both $\langle 111 \rangle \{110\}$ and $\langle 100 \rangle \{110\}$ slip systems in the NM and AF magnetic phases has been proposed with parameters extracted from *ab initio* calculations, where the contributions of the dislocation trajectory and relaxation volume are well defined. This criterion allowed to confirm the strong competition between $\langle 111 \rangle \{110\}$ and $\langle 100 \rangle \{110\}$ slip systems.

Additionally, we show in this study that this competition is even more pronounced including the influence of the orientation and sign of the mechanical loading. A particular zone of interest with respect to this observation lies close to $\langle 111 \rangle$ axis where $\langle 100 \rangle \{110\}$ slip systems are predicted to contribute to the plastic deformation of Cr. This result holds for both tensile and compressive loadings in the NM and AF magnetic phases. As a consequence, $\langle 100 \rangle$ screw dislocations should play an important role in the plastic deformation of bcc Cr.

Appendix A. Elastic constants of the dislocated crystal

Appendix A.1. $1/2\langle 111 \rangle$ screw dislocation

In section 3.1.3, the values of the elastic constants appearing in Eq. 1 for the extraction of the $1/2\langle 111 \rangle$ screw dislocations relaxation volume and trajectory had to be adjusted from the bulk values to ensure the following conditions on the dislocation core properties:

$$\begin{aligned} x(\xi = 0) &= 0 \\ x(\xi = 1) &= \lambda_P \\ \Delta\Omega_{12}(\xi = 0) &= \Delta\Omega_{12}(\xi = 1/2) = \Delta\Omega_{12}(\xi = 1) = 0 \end{aligned} \quad (\text{A.1})$$

In the frame of the $1/2\langle 111 \rangle$ screw dislocation, the elastic tensor appearing in Eq. 1 is:

$$\overline{\overline{C}}_{\langle 111 \rangle} = \begin{bmatrix} C_{11} & C_{12} & C_{13} & 0 & C_{15} & 0 \\ C_{12} & C_{11} & C_{13} & 0 & -C_{15} & 0 \\ C_{13} & C_{13} & C_{33} & 0 & 0 & 0 \\ 0 & 0 & 0 & C_{44} & 0 & -C_{15} \\ C_{15} & -C_{15} & 0 & 0 & C_{44} & 0 \\ 0 & 0 & 0 & -C_{15} & 0 & C_{66} \end{bmatrix}$$

To impose the above conditions A.1, only the C_{15} and C_{44} components of the elastic tensor have to be adjusted, by 6 GPa and 17 GPa respectively in the NM phase, and by 10 GPa and 17 GPa respectively in the AF phase (Tab. A.3). To test the validity of our approach, we evaluated the elastic constants of a simulation cell containing a dislocation dipole, and compared the results with the values for the perfect bcc unit cell. To do so, 6 different deformations are applied to both simulation cells, and the elastic constants are fitted to the *ab initio* stresses through a least-square minimization procedure. The calculation of the elastic constants of the dislocated crystal is carried out only for the NM magnetic phase, and the results are presented in Tab. A.3. Comparing the perfect bcc unit cell with the dislocated crystal, we find relatively small variations for the 7 components of the elastic tensor, except for C_{15} and C_{44} which vary by 5 GPa and 20 GPa respectively. This change is of the same order and sign than for the fitted elastic constants obtained through the procedure to impose the symmetry of the $1/2\langle 111 \rangle$ screw dislocation relaxation volume and trajectory in the NM magnetic phase. The adjustment of the elastic constants therefore appears legitimate in view of anharmonic effects induced by the dislocation dipole, a result already observed in bcc tungsten [17].

Appendix A.2. $\langle 100 \rangle$ screw dislocation

In the frame of the $\langle 100 \rangle$ screw dislocation, the elastic tensor is:

$$\overline{\overline{C}}_{\langle 100 \rangle} = \begin{bmatrix} C_{11} & C_{12} & C_{13} & 0 & 0 & 0 \\ C_{12} & C_{11} & C_{13} & 0 & 0 & 0 \\ C_{13} & C_{13} & C_{33} & 0 & 0 & 0 \\ 0 & 0 & 0 & C_{44} & 0 & 0 \\ 0 & 0 & 0 & 0 & C_{44} & 0 \\ 0 & 0 & 0 & 0 & 0 & C_{66} \end{bmatrix}$$

Only the conditions A.1 on the dislocation position has to be satisfied as Ω_{12} is null for $\langle 100 \rangle$ screw dislocation gliding in a $\{110\}$ plane. For this purpose,

Table A.3: Elastic constants (in GPa) of the perfect bcc unit cell rotated in the frame of the 1/2(111) screw dislocation (Perfect crystal), of the simulation cell containing the dislocation dipole (Dislocated crystal), and the corrected values used to extract the screw dislocation trajectory and variations of the relaxation volume (Fit).

NM phase	C_{11}	C_{12}	C_{13}	C_{15}	C_{33}	C_{44}	C_{66}
Perfect crystal	420	164	191	38	394	155	128
Dislocated crystal	416	174	195	33	382	135	118
Fit	420	164	191	32	394	138	128
AF phase	C_{11}	C_{12}	C_{13}	C_{15}	C_{33}	C_{44}	C_{66}
Perfect crystal	338	86	117	45	306	157	126
Fit	338	86	117	35	306	140	126

only C_{44} had to be slightly adjusted from the bulk values, as presented in Tab. A.4. The correction is only of a few GPa in both magnetic phases (4 GPa and 1 GPa in the NM and AF phases respectively).

Table A.4: Elastic constants (in GPa) of the bcc unit cell rotated in the frame of the (100) screw dislocation (Perfect) and the corrected values used to extract the screw dislocation trajectory and variations of the relaxation volume (Fit).

NM phase	C_{11}	C_{12}	C_{13}	C_{33}	C_{44}	C_{66}
Perfect	415	219	151	483	98	166
Fit	415	219	151	483	102	166
AF phase	C_{11}	C_{12}	C_{13}	C_{33}	C_{44}	C_{66}
Perfect	343	152	63	432	96	185
Fit	343	152	63	432	97	185

Acknowledgments

This work was performed using HPC resources from GENCI-CINES and -TGCC (Grants 2020-096847) and is funded by the French Tripartite Institute (CEA-EDF-Framatome) through the ICOMB project. We thank Dr. Chu-Chun Fu for fruitful discussions.

References

- [1] E. Fawcett, Spin-density-wave antiferromagnetism in chromium, *Rev. Mod. Phys.* 60 (1988) 209–283. doi:10.1103/RevModPhys.60.209.
- [2] A. C. McLaren, Dislocation Substructures in Deformed and Recovered Chromium, *Aust. J. Phys.* 17 (1964) 447–451. doi:10.1071/ph640447.
- [3] C. N. Reid, A. Gilbert, Dislocation structure in chromium, chromium-rhenium, and chromium-iron alloys, *J. Less Common Met.* 10 (1966) 77–90. doi:10.1016/0022-5088(66)90116-0.
- [4] K. F. Hale, M. H. Brown, Experimental determination of Burgers vectors of dislocations, *Proc. R. Soc. Lond. A* 310 (1969) 479–491. doi:10.1098/rspa.1969.0088.

- [5] J. Holzer, Z. Chlup, T. Kruml, R. Gröger, Plastic deformation of magnetically isotropic or single crystals compressed at 77 k, *Int. J. Plast.* 138 (2021) 102938. doi:10.1016/j.ijplas.2021.102938.
- [6] C. N. Reid, A. Gilbert, G. T. Hahn, Dislocation and deformation modes in chromium single crystals, *Trans. AIME* 239 (1967) 467–473.
- [7] B. Bienvenu, C. C. Fu, E. Clouet, Impact of magnetism on screw dislocations in body-centered cubic chromium, *Acta Mat.* 200 (2020) 570–580. doi:10.1016/j.actamat.2020.09.041.
- [8] M. J. Marcinkowski, H. A. Lipsitt, The plastic deformation of chromium at low temperatures, *Acta Met.* 10 (1962) 95–111. doi:10.1016/0001-6160(62)90055-X.
- [9] C. Reid, Dislocation widths in anisotropic b.c.c. crystals, *Acta Metall.* 14 (1966) 13–16. doi:10.1016/0001-6160(66)90266-5.
- [10] Y. T. Chou, Dislocation reactions and networks in anisotropic bcc crystals, *Mat. Sci. Eng.* 10 (1972) 81–86. doi:10.1016/0025-5416(72)90071-7.
- [11] J. W. Christian, Some surprising features of the plastic deformation of body-centered cubic metals and alloys, *Metall. Trans. A* 14 (1983) 1237–1256. doi:10.1007/BF02664806.
- [12] M. S. Duesbery, Z. S. Basinski, On non-glide stresses and their influence on the screw dislocation core in body-centred cubic metals I. The Peierls stress, *Proc. R. Soc. Lond. A* 392 (1984) 145–173. doi:10.1098/rspa.1984.0027.
- [13] M. S. Duesbery, V. Vitek, Plastic anisotropy in b.c.c. transition metals, *Acta Mat.* 46 (1998) 1481–1492. doi:10.1016/S1359-6454(97)00367-4.
- [14] M. H. A. Nawaz, B. L. Mordike, Slip Geometry of Tantalum and Tantalum Alloys, *Phys. Status Solidi A* 32 (1975) 449–458. doi:https://doi.org/10.1002/pssa.2210320213.
- [15] L. Dezerald, D. Rodney, E. Clouet, L. Ventelon, F. Willaime, Plastic anisotropy and dislocation trajectory in BCC metals, *Nat. Commun.* 7 (2016) 11695. doi:10.1038/ncomms11695.
- [16] A. Kraych, E. Clouet, L. Dezerald, L. Ventelon, F. Willaime, D. Rodney, Non-glide effects and dislocation core fields in BCC metals, *npj Computational Materials* 5 (2019) 1–8. doi:10.1038/s41524-019-0247-3.
- [17] E. Clouet, B. Bienvenu, L. Dezerald, D. Rodney, Screw dislocations in BCC transition metals: from ab initio modeling to yield criterion, *C. R. Phys.* 22 (2021) 1–34. doi:10.5802/crphys.75.
- [18] G. Kresse, J. Furthmüller, Efficiency of ab-initio total energy calculations for metals and semiconductors using

- a plane-wave basis set, *Comput. Mater. Sci.* 6 (1996) 15–50. doi:10.1016/0927-0256(96)00008-0.
- [19] J. P. Perdew, K. Burke, M. Ernzerhof, Generalized Gradient Approximation Made Simple, *Phys. Rev. Lett.* 77 (1996) 3865–3868. doi:10.1103/PhysRevLett.77.3865.
- [20] R. Hafner, D. Spišák, R. Lorenz, J. Hafner, Magnetic ground state of Cr in density-functional theory, *Phys. Rev. B* 65 (2002) 184432. doi:10.1103/PhysRevB.65.184432.
- [21] V. Vanhoof, M. Rots, S. Cottenier, Spin-density wave in Cr: Nesting versus low-lying thermal excitations, *Phys. Rev. B* 80 (2009) 184420. doi:10.1103/PhysRevB.80.184420.
- [22] R. Soulaïrol, C.-C. Fu, C. Barreateau, Structure and magnetism of bulk Fe and Cr: from plane waves to LCAO methods, *J. Phys.: Condens. Matter* 22 (2010) 295502. doi:10.1088/0953-8984/22/29/295502.
- [23] S. Cottenier, B. D. Vries, J. Meersschant, M. Rots, What density-functional theory can tell us about the spin-density wave in Cr, *J. Phys.: Condens. Matter* 14 (2002) 3275–3283. doi:10.1088/0953-8984/14/12/314.
- [24] D. Rodney, L. Ventelon, E. Clouet, L. Pizzagalli, F. Willaime, Ab initio modeling of dislocation core properties in metals and semiconductors, *Acta Mat.* 124 (2017) 633–659. doi:10.1016/j.actamat.2016.09.049.
- [25] E. Clouet, Ab Initio Models of Dislocations, in: W. Andreoni, S. Yip (Eds.), *Handbook of Materials Modeling : Methods: Theory and Modeling*, Springer International Publishing, 2018, pp. 1–22. doi:10.1007/978-3-319-42913-7_22-1.
- [26] L. Dezerald, L. Ventelon, E. Clouet, C. Denoual, D. Rodney, F. Willaime, Ab initio modeling of the two-dimensional energy landscape of screw dislocations in bcc transition metals, *Phys. Rev. B* 89 (2014) 024104. doi:10.1103/PhysRevB.89.024104.
- [27] V. Vitek, M. Mrovec, J. L. Bassani, Influence of non-glide stresses on plastic flow: from atomistic to continuum modeling, *Mat. Sci. Eng. A* 365 (2004) 31–37. doi:10.1016/j.msea.2003.09.004.
- [28] R. Gröger, A. G. Bailey, V. Vitek, Multiscale modeling of plastic deformation of molybdenum and tungsten: I. Atomistic studies of the core structure and glide of $1/2\langle 111 \rangle$ screw dislocations at 0K, *Acta Mat.* 56 (2008) 5401–5411. doi:10.1016/j.actamat.2008.07.018.
- [29] R. Gröger, V. Racherla, J. L. Bassani, V. Vitek, Multiscale modeling of plastic deformation of molybdenum and tungsten: II. Yield criterion for single crystals based on atomistic studies of glide of $1/2\langle 111 \rangle$ screw dislocations, *Acta Mat.* 56 (2008) 5412–5425. doi:10.1016/j.actamat.2008.07.037.
- [30] R. Gröger, V. Vitek, Single crystal yield criterion for chromium based on atomistic studies of isolated $1/2\langle 111 \rangle$ screw dislocations, *Int. J. Plast.* 132 (2020) 102733. doi:10.1016/j.ijplas.2020.102733.
- [31] R. I. Garrod, H. L. Wain, Dislocation arrangements and brittleness in chromium, *J. Less Common Met.* 9 (1965) 81–94. doi:10.1016/0022-5088(65)90086-X.